Original

Laipple, D.; Stark, A.; Schimanski, F.-P.; Schwebke, B.; Pyczak, F.; Schreyer, A.:

Microstructure of Ti-45Al-5Nb and Ti-45Al-10Nb powders

Microstructure of Ti-45Al-5Nb and Ti-45Al-10Nb powders

Daniel Laipple[1,a*], Andreas Stark[1,b], Frank-Peter Schimansky[1,c],
Bernd Schwebke[1,d], Florian Pyczak[1,e] and Andreas Schreyer[1,f]

[1] Helmholtz-Zentrum Geesthacht, 21502 Geesthacht, Germany

[a]daniel.laipple@hzg.de, [b]andreas.stark@hzg.de, [c]frank-peter.schimansky@hzg.de,
[d]bernd.schwebke@hzg.de, [e]florian.pyczak@hzg.de, [f]andreas.schreyer@hzg.de

Abstract. Gas-atomised spherical powders of Ti-45Al-5Nb and Ti-45Al-10Nb alloys were produced using the plasma melting induction guided gas atomisation (PIGA) technique. The phase composition was determined by X-ray diffraction at the synchrotron beamline HEMS at PETRA III (DESY), as well as by scanning electron microscopy (SEM), energy dispersive X-ray spectroscopy (EDX), two dimensional and focused ion beam (FIB) based three dimensional electron back scatter diffraction (EBSD) measurements. Due to the high cooling rates the alloy composition of both alloys consists of hexagonal-close-packed α- and body-centred-cubic β-phase. The α-phase is dominant in the larger powder size fractions. Considerable amounts of the β phase were only found in the powder particle size fractions smaller than 32 μm for the Ti-45Al-5Nballoy and smaller than 45 μm for the Ti-45Al-10Nb. A pronounced dendritic cauliflower-like structure was observed in bigger powder particles of the Ti-45Al-10Nb alloy. This gives proof that diffusion took place during the initial β-grain formation, even though there is no orientation relation between the final grain and the dendrite structure in the powder particles. The presence of dendritic structures showed that the cooling rate during powder atomization was still too low to reach the critical growth rate for a planar solidification. The absence of preferred misorientation angles between α-grains indicates that α-grains are not formed out of already solidified β-grains by a solid state phase transformation.

1. Introduction

Gas atomisation is a process which produces metallic powder particles far from equilibrium due to the inherent high cooling rates. Usually a more or less broad distribution of powder particle sizes results and the actual cooling rate varies with powder particle size. For multiphase materials with a relatively complex phase diagram, undergoing a number of solid state phase transformations between solidification and room temperature, different powder particle sizes may provide snapshots of rapidly quenched non-equilibrium microstructures for different cooling rates. Such differences in the microstructure of different powder particle size fractions may influence later processing steps by altering diffusion rates or mechanical properties. In this study different powder particle size fractions of TiAl alloys, an upcoming material for aeronautic and automotive applications at elevated temperatures, were microstructurally characterised by different advanced microscopy and diffraction methods. Gas-atomised spherical powders of Ti-45Al-5Nb and Ti-45Al-10Nb (in at.%) alloys were produced using the plasma melting induction guided gas atomisation (PIGA) technique. The powder size fraction <180 μm was subsequently hot isostatically pressed (HIPed) at 200 MPa for 2 h at 1250 °C. These powder compacts were microstrucurally and homogeneous and were used as starting material for many experiments and pre-tests of industrial processing routes [1, 2, 3]. In the as-HIPed condition Ti-45Al -5Nb consists of 75 vol.% γ-TiAl and 25 vol.% α2-Ti3Al whereas Ti-45Al-10Nb consists of 83 vol.% γ-TiAl, 8 vol.% α2-Ti3Al and 9vol.% ωo-Ti4Al3Nb [4]. The general solidification sequence for binary TiAl alloys is L→L+β→(β)→α+β→α→α+γ→α2+γ [5]. However, the addition of Nb stabilises the β phase and increases the possible phase transformation pathways [6]. Thus, many different microstructures can be adjusted in bulk TiAl materials depending on the applied heat treatment [5, 7].

To our knowledge, this study is the first detailed investigation of the powder particles of Nb-rich TiAl alloys directly after atomisation. The study is focused on the influence of the high cooling rate on phase composition and microstructures formed after quenching.

2. Experimental

2.1. Powder preparation by PIGA. A melt is generated by means of an Ar-operated plasma torch in a water cooled Cu crucible. The desired alloy composition is achieved by combining appropriate weights of pure metals for the first melting step. To ensure chemical homogeneity the alloy button is re-melted up to four times prior to powder atomization. Subsequently the melt is guided by a funnel to the center of a gas nozzle where it becomes atomised using Ar gas [8]. By this technique varying amounts of different sized particles are generated as shown in Table 1.

Table 1: Mesh analysis in mass percent of Ti-45Al-5Nb powder produced by PIGA.

diameter [μm]	[%]
<20	4.40
20-32	6.39
32-45	8.43
45-63	11.94
63-90	15.71
90-125	19.71
125-180	18.21
180-250	10.65
250-355	4.57

2.2. Characterisation by SEM imaging techniques & EDX. A crossbeam workstation AURIGA 40 from Zeiss (Oberkochen, Germany) was used for scanning electron microscopy (SEM) investigations. It combines a SEM with a focused ion beam (FIB) column in one device. For the investigations the powders were deposited on a sample holder brushed with silver glue. For energy dispersive X-ray spectroscopy (EDX) the device Apollo XP from EDAX (Ametek GmbH, Wiesbaden, Germany) was used. The measurement and analysis was operated by the software Genesis Spectrum (Version 6.255) from EDAX.

2.3. Phase composition by X-ray diffraction. High-energy X-ray diffraction (HEXRD) was performed for the Ti-45Al-5Nb and Ti-45Al-10Nb powders at the HEMS-beamline at PETRA III (DESY). The powder particles of the different size fractions were filled in glass tubes with an inner diameter of 4 mm. A photon energy of 87 keV and a beam size of 0.5×0.5 mm were used for HEXRD. The Debye-Scherrer-rings were recorded with a Mar345 detector. The diffraction data was processed using the software fit2D (V12.077) from A. Hammersley, ESRF (Grenoble, France) while the subsequent data evaluation by Rietveld analysis was done with powdercell 2.4 from Federal Institute for Materials Research and Testing (BAM) (Berlin, Germany).

2.4. 2D & 3D EBSD on single particles. For EBSD the DigiView detector from EDAX was used. Data acquisition and analysis is accomplished by the EDAX software TSL-OIM. 2D EBSD mappings on FIB processed cross sections were performed on single particles of the Ti-45Al-10Nb alloy with diameters of roughly 20, 40 and 100 μm. The applied FIB acceleration voltage of 30 kV on all samples induced negligible FIB amorphisation damage. Although experiments by T. L. Matteson et.al found a better EBSD signal quality on FIB cross sections milled by lower FIB acceleration voltages [9], the resulting signal enabled the crystal labelling of the surface very well. Furthermore a better image quality was obtained by using comparably higher ion currents of some nano Ampere. The crossbeam workstation Auriga together with the EDAX software TSL-OIM provides 3D-EBSD too. Several 3D EBSD measurements on different powder particles of the Ti-45Al-10Nb alloy could be performed in adequate times, which still means on the scale of days. The measurements were performed at up to 20 kV electron high tension (U_{EHT}).

2.5. EBSD on embedded powder fractions. To enhance the statistics of the phase composition measurements by EBSD, embedding and cross sectioning was performed, featuring a larger scan area with many single particle cross sections at once. The powder fractions <20 μm, 20-32 μm and 90-125 μm of the Ti-45Al-10Nb alloy were selected and embedded in a conductive epoxy resin, consecutively grinded with 1200 and 2500 μm grained paper and finally polished by hand using a SiO$_2$ solution on a polishing disc wheel. Again the EBSD measurements were done at 20 kV U$_{EHT}$.

3. Results and discussion

3.1. Characterisation by SEM imaging techniques & EDX. All powder particle size fractions of the two alloys, Ti-45Al-5Nb and Ti-45Al-10Nb, were investigated by SEM imaging (Fig. 1 (a) & (b)). A cauliflower-like structure was detected on the surface of the particles, which is almost equally sized and independent of the particle diameter. By cross sectioning of embedded particles and investigating using backscattered electron (BSE) contrast the continuation of these surface structures was detected as dendrites throughout the entire particles. This is shown for Ti-45Al-10Nb in Fig. 1 (c) & (d). The structures in the powder particles stem from an inhomogeneous distribution of the alloying elements and imply that no planar solidification occurred. To determine the composition differences of this dendrite structures, EDX point measurements at 20 kV U$_{EHT}$ were performed on darker (interdendritic) and brighter (dendrite core) regions of the BSE-images of the Ti-45Al-10Nb alloy in Fig. 1. The elemental composition in at.% of a dark region of the 12 μm particle shown in Fig. 1 (c) is Ti-46.02Al-8.70Nb, while a bright region was determined to be Ti-44.95Al-9.76Nb. For a darker region of the 80 μm particle shown in Fig. 1 (d), the elemental composition was determined to be Ti-48.73Al-6.66Nb, while a bright region exhibited a composition of Ti-44.46Al-10.42Nb. Obviously the bigger 80 μm particle features larger differences of its Nb distribution in the dendritic structures. Furthermore, the average Nb content of the smaller 12 μm particle is significantly lower compared to the nominal composition of Ti-45Al-10Nb, while it is only slightly higher for the larger particle.

A complementary EDX-mapping performed on the cross sections of these two particles is shown in Fig. 1 (e) & (f). The elemental contrast by Nb for the dendrites is hardly visible for the 12 μm particle. The dendritic structure of bigger particles of the Ti-45Al-10Nb alloy is more pronounced, while smaller particles seem to contain in average less pronounced Nb inhomogeneities. The dendritic structures in the powder particles highlight an unequal distribution of the alloy's elements and imply that no planar solidification occurred. Hence, even for a small particle with less than 20 μm diameter the cooling rate by gas atomisation with Ar, which can roughly be estimated to be 10^6 K/s [10] was still too low to reach the critical growth rate for planar solidification. It was found that the dendritic cauliflower-like structures of bigger particles of Ti-45Al-10Nb are more pronounced than for the Ti-45Al-5Nb alloy.
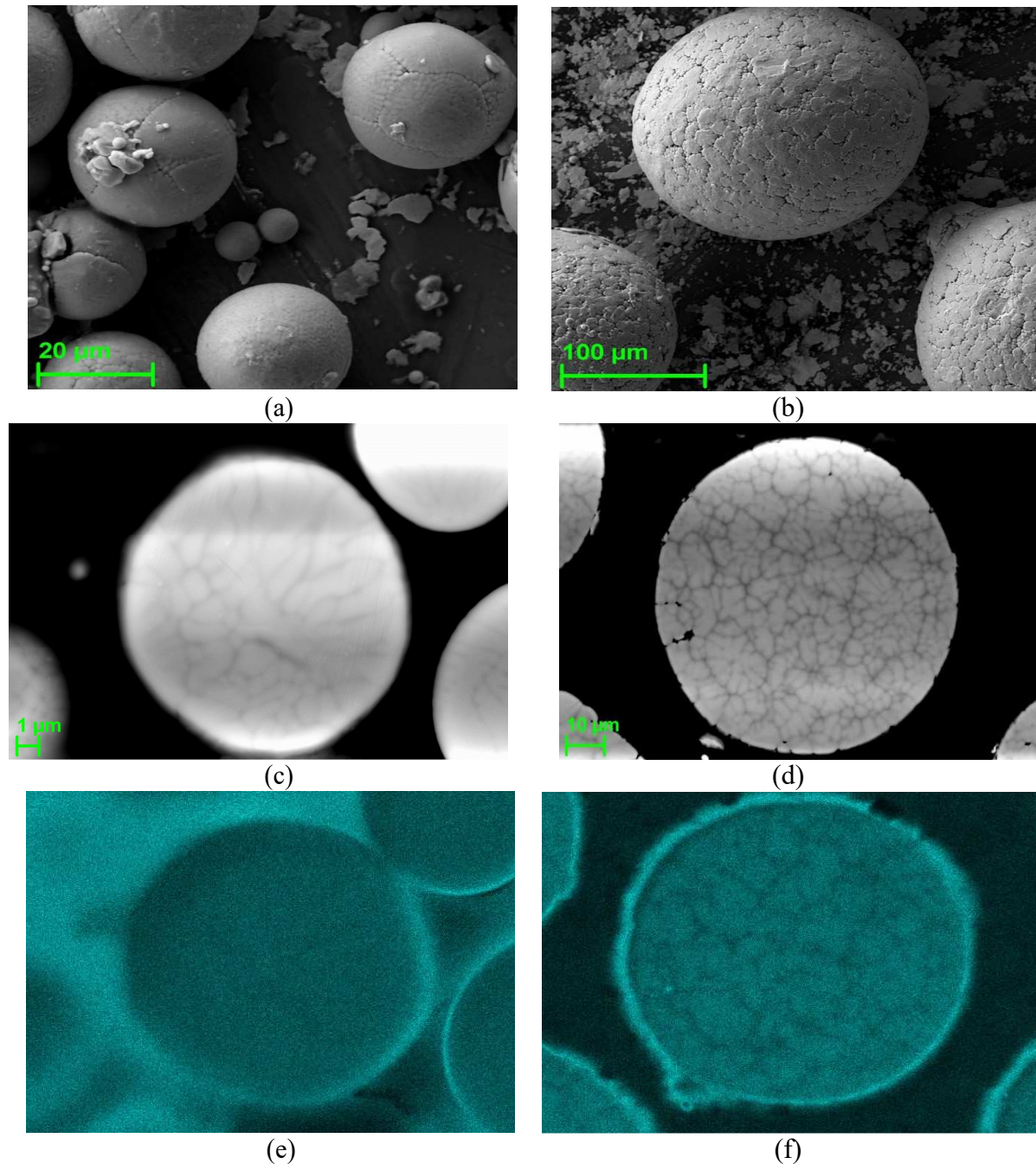
Figure 1: SEM images of Ti-45Al-10Nb powder of the fractions 20-32 μm (a) and 180-250 μm (b); 15 kV U$_{EHT}$, 5 mm WD, SE2-detector. Cross sections with dendrite structures of (c) 12 μm and (d) 80 μm particles (diameter), with corresponding EDX-mappings (e) & (f) respectively; 20 kV U$_{EHT}$, 8.5 mm WD, BSE-detector, EDX was performed at 20 kV U$_{EHT}$.

3.2. Phase composition by Powder diffraction. The determined phase compositions are shown in Fig. 2. The data-set shows an increased amount of α-phase with increasing particle diameter. This is caused by the decreased cooling rate of the bigger gas-atomised powder particles, providing more time to reach a lower temperature phase constitution containing more α-phase. The Ti α phase is the dominant phase constituent in almost every powder particle size fraction that was investigated, except for <20 μm. In the Ti-45Al-5Nb alloy one finds considerable amounts of the β phase only in size fractions smaller than 32 μm. For the Ti-45Al-10Nb alloy this was qualitatively similar but for powder fractions smaller than approximately 45 μm. The total β phase amount in Ti-45Al-10Nb for the same size fractions was generally higher than in Ti-45Al-5Nb, as expected for a higher Nb content [1].
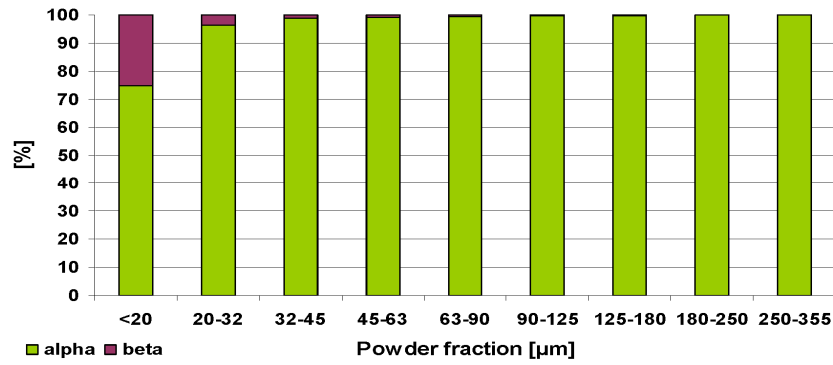
(a) Phase distribution of 5Nb powder fractions
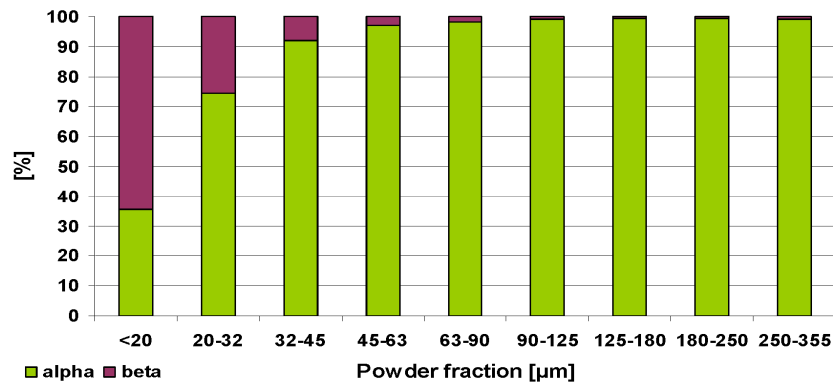
(b) Phase distribution of 10Nb powder fractions

Figure 2: TiAl-α and -β phase composition of Ti-45Al-5Nb & Ti-45Al-10Nb powder fractions in volume percent. The data was obtained by Rietveld analysis of diffraction patterns.

The larger particle size fractions of 180-250 µm and 250-355 µm show furthermore slight peaks of the ordered phase α2 (Fig. 3). Again this can be attributed to the decreased cooling rate, because the transformation from disordered α- to ordered α2-phase occurs at lower temperatures. The peaks of the α2-phase are slightly more pronounced in the Ti-45Al-5Nb alloy. This effect is probably caused by the lower Nb amount in the Ti-45Al-5Nb alloy, not restraining the diffusion processes which are necessary to facilitate the transformation of the α2-phase out of α.

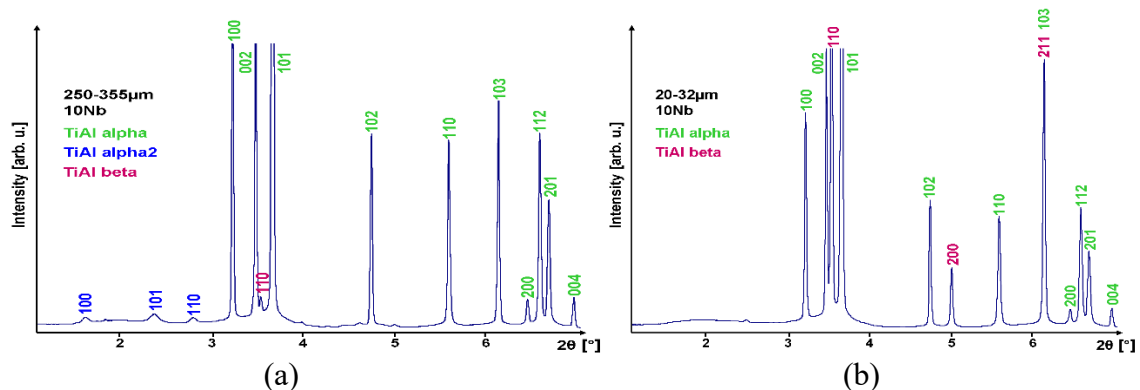Figure 3: Diffraction patterns of the Ti-45Al-10Nb alloy: (a) 20-32 µm particle size fraction (74.5% α- / 25.5% β-phase); (b) 250-355 µm particle size fraction (99.2% α- / 0.8% β-phase, superlattice peaks of the α2-phase).

3.3. 2D & 3D EBSD on single particles. In Fig. 4 the α-phase grain structure of a powder particle with 100 µm diameter is presented in three dimensions. The EBSD slices as well as the scan points of the single EBSD mappings are both distanced by 600 nm. In this figure the scan points are interpolated between the slices, using the tomography software Avizo Fire from the

visualisation sciences group (VSG) (Mérignac Cedex, France). The isolation of the bright green α-phase grain was done by a so called watershed transformation on accordingly selected, grey valued voxels, again performed with Avizo. It shows a compound of an apparently arbitrary grown α-phase grain. A preferred growth direction could not be determined and the grains even grew partially around each other. The grains are not arranged in accordance to the cauliflower-like structures detected by BSE inside the particles and no preferred crystal orientations with respect to the shape of the powder particle could be determined.
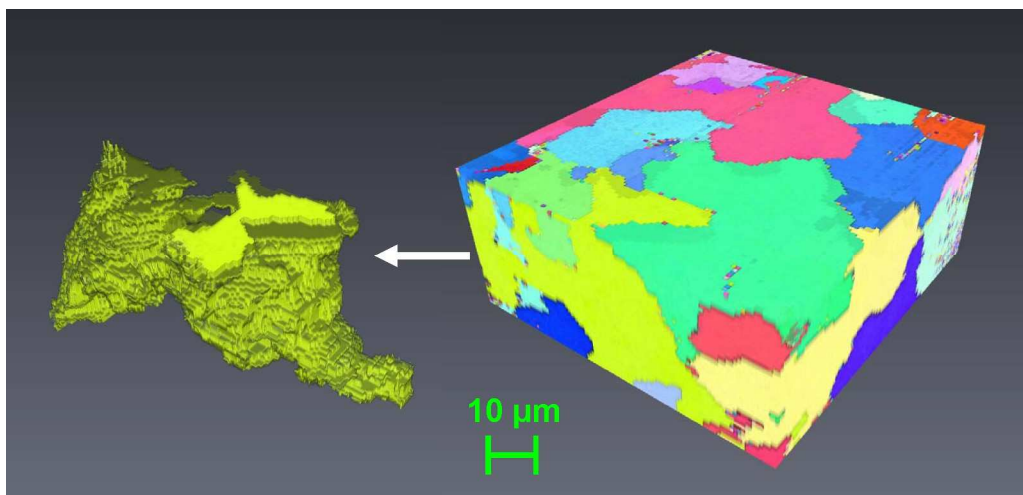

Figure 4: Cropped cube of 3D α-phase grain structure of a 100 μm sized Ti-45Al- 10Nb particle, sliced by a 2 nA FIB current. Each grain is arbitrary but uniquely coloured. The green grain (left side) was isolated out of the entire 3D body.

3.4. EBSD on embedded powder fractions. The powder diffraction already revealed an increased β-phase amount for the smaller particle size fractions. Therefore the powder fractions <20 μm, 20-32 μm and 90-125 μm of the Ti-45Al-10Nb alloy were selected. The mapping of the 20-32 μm fraction was done on a larger region to obtain a comparable particle statistic regarding the <20 μm fraction. In order to determine the ratio of α- to β- phase in the EBSD phase images the noise in the area between the particles had to be set to a homogeneous value like black. This was done using the EDAX software TSL-OIM-Analysis 5.31. All pixels of the respective EBSD scan were indexed by a so called cleanup with a confidence value, calculated from the misorientations of the surrounding pixels. Subsequently a partitioning of the data was performed by setting a threshold to the confidence index, which resulted in a phase image without noise, shown in Fig. 5.
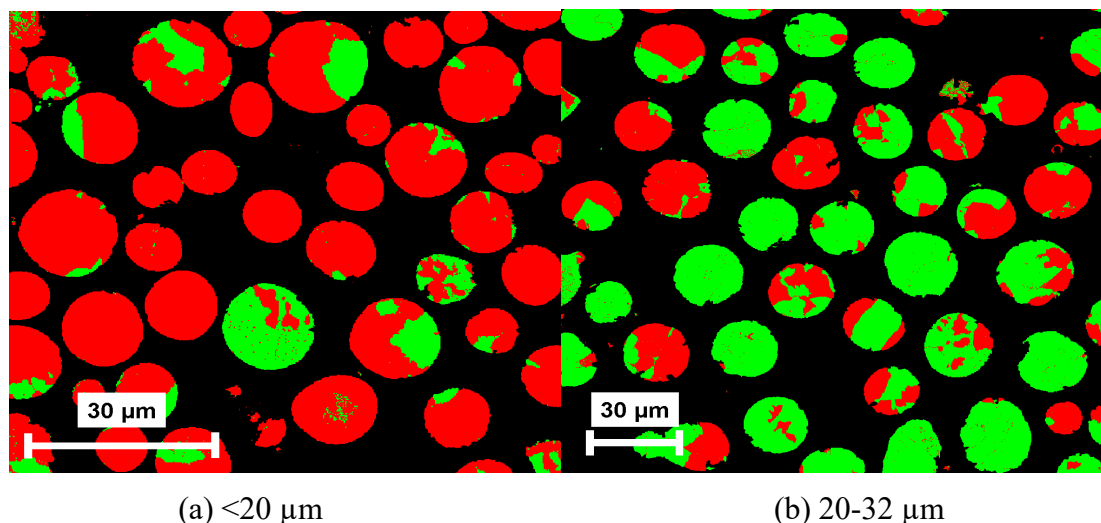

(a) <20 μm   (b) 20-32 μm

Figure 5: EBSD mappings of resin embedded Ti-45Al-10Nb powder fraction cross sections; α-phase (green) and β-phase (red).

3.4. EBSD on embedded powder particles. The phase fractions of the <20 μm and 20-32 μm size fraction were determined from the image already shown in Fig. 5. The phase contents of the <20 μm size fraction are 14.7% α- and 85.3% β-phase, respectively, while the 20-32 μm size fraction exhibited 64.1% α- and 35.9% β-phase. Both values are higher by 10 - 20% for the β-phase than obtained by the diffraction measurements. However, this could be explained by the lower statistics compared to diffraction. Besides, numerous particles contain α-phase grain and β-phase grains as well. The 90-125 μm powder particle size fraction EBSD scan of the Ti-45Al-10Nb alloy was also processed by the described noise cleanup using the EDAX software. The phase composition given in Fig. 6 (a) shows only 0.4 % β-phase amount in accordance with the results of the powder diffraction measurements. The β-phase is only present in very small satellite particles and no β-phase grains are present in big particles. In Fig. 6 (b) again no preferred crystal grain orientations are present.
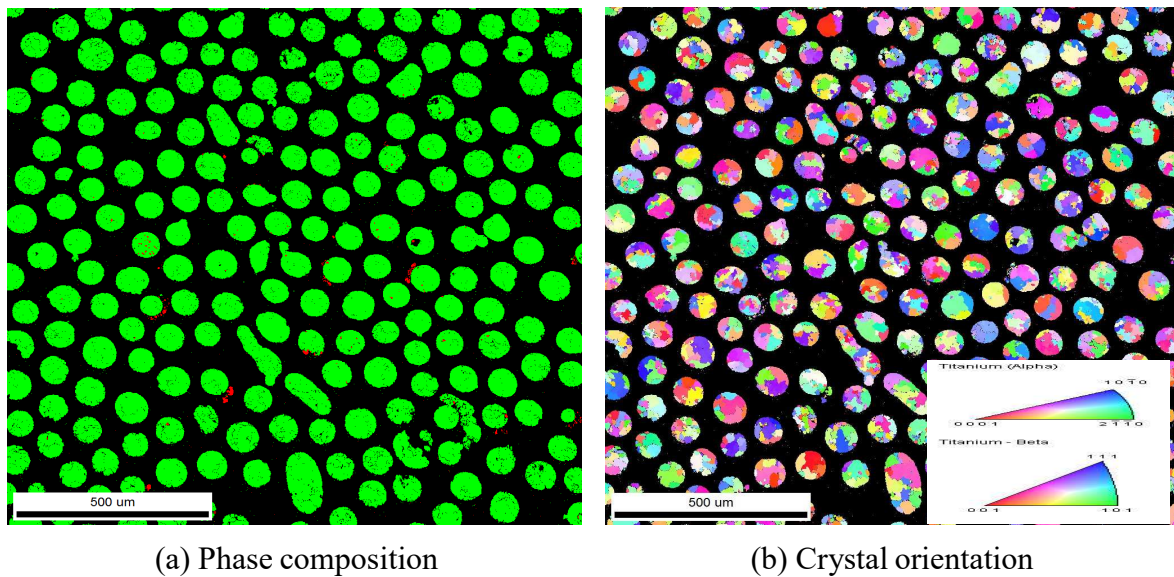

(a) Phase composition   (b) Crystal orientation

Figure 6: Phase composition of the Ti-45Al-10Nb alloy 90-125 μm powder particle size fraction, α-phase (green) and β-phase (red) (a). Grain orientation map of the α-phase (b).

The Ti-α-phase grains are usually supposed to be transformed out of Ti-β-phase grains [11]. When the Ti-β → Ti-α transformation obeys the Burgers orientation relationship [12] each Ti-β orientation would result in 12 possible Ti-α orientations. The α-grains growing from the same parent β-grain are thus characterised by related misorientation angles. Gey and Humbert showed that for grains which stem from the same parent Ti-β grain the misorientation angles 10°53', 60°, 60°83', 63°26' or 90° are measured for neighbouring Ti-α grains [13]. Therefore the misorientation of neighbouring α-grains was evaluated for the performed EBSD scan of the 90-125 μm size fraction, depicted in Fig. 7. However, no preferred misorientation angle could be detected, as already the 3D image of one powder particle in Fig. 3 indicated. Hence, one finds that the α-grains are not formed out of already solidified β-grains according the Burgers relationship by a solid state phase transformation.
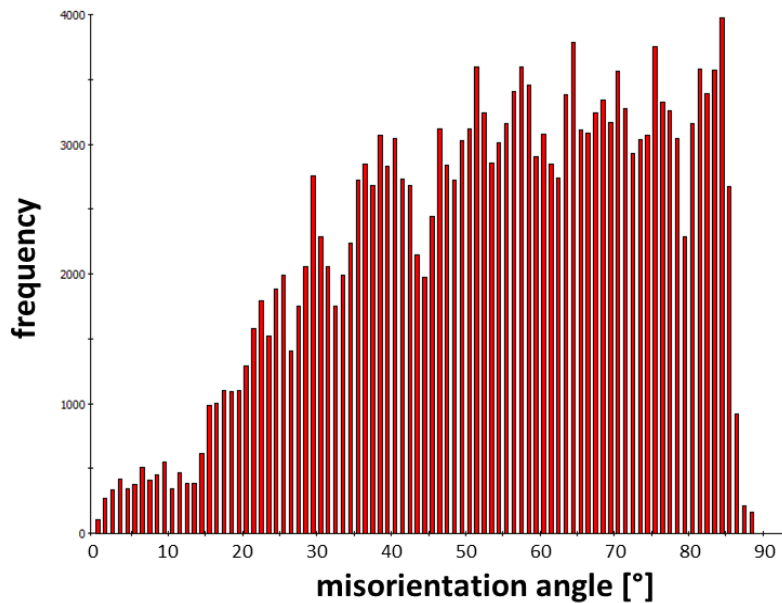
Figure 7: Misorientation histogram of neighbouring α-grains of the Ti-45Al-10Nb alloys 90-125 μm powder fraction from EBSD scan (compare Fig. 7 (b)).

For both alloy compositions under investigation initially β-grains should form out of the melt during solidification [14]. The dendritic structure gives proof that diffusion took place during solidification and initial β-grain formation, even though there is no relation between the grains and the dendrite structure. By the absence of preferred misorientation angles one finds that α-grains are not formed out of already solidified β-grains according the Burgers relationship by a solid state phase transformation. It has to be assumed that the hexagonal-close-packed α-phase was generated already out of the melt by a peritectic reaction or that by the relatively fast cooling rates a nucleation of α phase in the β grains which obeys the Burgers orientation relationship is supressed.

4. Conclusions.

Except for the <20 μm fractions the Ti α-phase is the dominant fraction in every powder fraction that was investigated. Regarding the Ti-45Al-5Nb alloy one finds considerable amounts of the β-phase only in fractions smaller than 32 μm. For the Ti-45Al-10Nb alloy this was similar, but for powder fractions smaller than approximately 45 μm. The total β-phase amount in Ti-45Al-10Nb fractions was generally higher, as expected for a higher Nb content [7]. It was found that the dendritic cauliflower-like structures of bigger particles of Ti-45Al-10Nb are more pronounced than for the Ti-45Al-5Nb alloy. The presence of dendritic structures showed that the cooling rate during powder atomization was still too low to reach the critical growth rate for absolute stability and thus a planar solidification. By the absence of preferred misorientation angles one finds that α-grains are not formed out of already solidified β-grains according the Burgers relationship [12] by a solid state phase transformation.
Finally, initial β-grains were formed out of the melt during cooling, since the β-phase is generally preferred to be primarily formed [14]. The BSE detected cauliflower structure is giving proof that diffusion took place during solidification of the initial β-grain formation, even though there is no relation between the grains and the dendrite structure. The grain formation started from the cooler surface by several seeds, growing chaotically into the particle. Regarding the occurring, still extremely fast cooling rates of 10^6 K/s [10], the hexagonal-close-packed α-phase is possibly originated by a martensitic phase transition from the body-centered-cubic β-phase. However, a significant orientation relationship of the α-grains is missing. Presumably the α-phase was formed in parallel to the β-phase in the region of the phase diagram [6] where both phases occur likewise, regarding the respective particles cooling rates.

References

[1] R. Gerling, F.-P. Schimansky, A. Stark, A. Bartels, H. Kestler, L. Cha, C. Scheu, and H. Clemens, Microstructure and mechanical properties of Ti 45Al 5Nb + (0-0.5C) sheets, Intermetallics, 16 (2008), pp. 689–697.

[2] A. Stark, A. Bartels, H. Clemens, S. Kremmer, F.-P. Schimansky, and R. Gerling, Microstructure and Texture Formation During Near Conventional Forging of an Intermetallic Ti-45Al-5Nb Alloy, Advanced Engineering Materials, 11 (2009), pp. 976–981.

[3] A. Stark, M. Oehring, F. Pyczak, and A. Schreyer, In situ observation of various phase transformation paths in Nb-rich TiAl alloys during quenching with different rates, Advanced Engineering Materials, 13 (2011), pp. 700-704.

[4] A. Stark, Textur- und Gefügeentwicklung bei der thermomechanischen Umformung Nb-reicher Gamma-TiAl-Basislegierungen, Shaker Verlag, Germany, 2010.

[5] F. Appel, J.D.H. Paul, and M. Oehring, Gamma titanium aluminide alloys: science and technology, Wiley-VCH Weinheim, Germany, 2011.

[6] V. T. Witusiewicz, A. A. Bondar, U. Hecht, and T. Y. Velikanova, The Al-B-Nb-Ti system. IV. Experimental study and thermodynamic re-evaluation of the binary Al-Nb and ternary Al-Nb-Ti systems, Journal of Alloys and Compounds, 472 (2009), pp. 133–161.

[7] H. Clemens and S. Mayer, Design, Processing, Microstructure, Properties, and Applications of Advanced Intermetallic TiAl Alloys, Advanced Engineering Materials, 15 (2013), pp. 191–215.

[8] R. Gerling, H. Clemens, and F. P. Schimansky, Powder metallurgical processing of intermetallic gamma titanium aluminides, Advanced Engineering Materials, 6 (2004), pp. 23–38.

[9] T. L. Matteson, S. W. Schwarz, E. C. Houge, B. W. Kempshall, and L. A. Giannuzzi, Electron backscattering dffraction investigation of focused ion beam surfaces, Journal of Electronic Materials, 31 (2002), pp. 33–39.

[10] F.-P. Schimansky, G. Müllauer, and R. Gerling, Maßnahmen zur Erzielung großer Abkühlgeschwindigkeiten und kurzer Erstarrungszeiten in der Pulvermetallurgie, GKSS-Forschungszentrum Geesthacht GmbH, 1993.

[11] U. Hecht, V. Witusiewicz, A. Drevermann, and J. Zollinger, Grain refinement by low boron additions in niobium-rich TiAl-based alloys, Intermetallics, 16 (2008), pp. 969–978.

[12] W. G. burgers, On the process of transition of the cubic-body-centered modification into the hexagonal-close-packed modification of zirconium, Physica, 1 (1934), pp. 561–586.

[13] N. Gey and M. Humbert, Characterization of the variant selection occurring during the alpha ->beta ->alpha phase transformations of a cold rolled titanium sheet, Acta Materialia, 50 (2002), pp. 277–287.

[14] J. J. Valencia, C. Mccullough, C. G. Levi, and R. Mehrabian, Solidification Microstructure of Supercooled Ti-Al Alloys Containing Intermetallic Phases, Acta Metallurgica, 37 (1989), pp. 2517–2530.